



RESEARCH ARTICLE

10.1029/2021JD035842

Key Points:

- Spectra of gravity waves in the Antarctic mesosphere are examined through an analysis of 5-year all-sky OH airglow images
- Effects of wind filtering on slowly propagating gravity waves are shown through wind-blocking diagrams
- Eastward and southeastward propagating mesospheric gravity waves in winter and spring can be generated near the stratopause

Supporting Information:

Supporting Information may be found in the online version of this article.

Correspondence to:

Y.-S. Kwak,
yskwak@kasi.re.kr

Citation:

Kam, H., Song, I.-S., Kim, J.-H., Kim, Y. H., Song, B.-G., Nakamura, T., et al. (2021). Mesospheric short-period gravity waves in the Antarctic Peninsula observed in all-sky airglow images and their possible source locations. *Journal of Geophysical Research: Atmospheres*, 126, e2021JD035842. <https://doi.org/10.1029/2021JD035842>

Received 9 SEP 2021
Accepted 14 DEC 2021

Mesospheric Short-Period Gravity Waves in the Antarctic Peninsula Observed in All-Sky Airglow Images and Their Possible Source Locations

Hosik Kam¹ , In-Sun Song² , Jeong-Han Kim³ , Yong Ha Kim⁴ , Byeong-Gwon Song³ , Takuji Nakamura^{5,6} , Yoshihiro Tomikawa^{5,6} , Masaru Kogure⁷ , Mitsumu K. Ejiri^{5,6} , Septi Perwitasari⁸ , Masaki Tsutsumi^{5,6} , and Young-Sil Kwak^{1,9} 

¹Space Science Division, Korea Astronomy and Space Science Institute, Daejeon, South Korea, ²Mathematical Atmospheric Physics Lab, Department of Atmospheric Sciences, Yonsei University, Seoul, South Korea, ³Division of Polar Climate Sciences, Korea Polar Research Institute, Incheon, South Korea, ⁴Department of Astronomy, Space Science and Geology, Chungnam National University, Daejeon, South Korea, ⁵National Institute of Polar Research, Tokyo, Japan, ⁶Department of Polar Science, SOKENDAI (The Graduate University for Advanced Studies) Tokyo, Kanagawa, Japan, ⁷Department of Earth and Planetary Science, Kyushu University, Fukuoka, Japan, ⁸National Institute of Information and Communications Technology, Tokyo, Japan, ⁹Department of Astronomy and Space Science, Korea University of Science and Technology, Daejeon, South Korea

Abstract This study presents an analysis of OH airglow images observed from an all-sky camera (ASC) at King Sejong Station (KSS), Antarctic for the 2012–2016 period. The two-dimensional power spectra of short-period gravity waves (<1 hr) as a function of phase velocities are obtained using the M-transform method that employs the time sequence of ASC images. The amplitudes of the power spectral densities show that the mesospheric wave activity is the largest during winter (May, June, and July) and is the smallest in fall (February, March, and April). Wind-blocking diagrams are constructed on the same two-dimensional domain as in the two-dimensional spectra using horizontal winds obtained from MERRA-2 reanalysis at $z = 0–80$ km and from KSS meteor radar data at $z = 80–90$ km. Climatologically, the spectral regions of slowly propagating gravity waves (<30 m s⁻¹) are overlaid by the wind-blocking areas, which suggests the filtering of gravity waves with small phase speeds by winds below the upper stratosphere. Eastward propagating gravity waves in winter and intense south-eastward waves in spring (October) are found to be unfiltered by the stratospheric winds. It is also found from the spectral analysis that these unfiltered gravity waves can originate from the upper stratosphere or the lower mesosphere, and not from the troposphere, which suggests the possibility of ASC observation of the secondary gravity waves generated near the stratopause.

1. Introduction

Dynamics in the mesosphere and lower thermosphere (MLT) region are substantially influenced by energy and momentum transport from the lower atmosphere through vertically propagating atmospheric gravity waves (GWs). GWs can be generated by orography, convection, wind shear, fronts, and jet streams in the lower atmosphere (Fritts & Alexander, 2003; Kim et al., 2003) and can propagate to the MLT region without serious dissipation. In the MLT region, GWs can break gravitationally, and momentum deposition due to GW breaking induces acceleration or deceleration of the zonal wind in the mid-to high-latitude regions of each hemisphere. The GW momentum deposition subsequently forms the pole-to-pole mass circulations across two hemispheres which make cold summer and warm winter mesopauses at high latitudes (Becker, 2012; Fritts & Alexander, 2003; Lindzen, 1981).

Various observational and modeling studies have revealed that GW activities are particularly intense in what has been called a “GW hot spot” region over the Southern Andes and the Antarctic Peninsula, in which King Sejong Station (KSS; 62°S, 58°W) is located (Alexander & Teitelbaum, 2007; Baumgaertner & McDonald, 2007; Ern et al., 2004; Hindley et al., 2015; Kogure et al., 2020, 2021; Lee et al., 2013; Song et al., 2017, 2021). This region is characterized by steep topography, strong winds over the Southern Ocean, and vigorous frontal activities that are responsible for strong orographic, convective, and jet-front gravity waves. In this region, GWs can interact directly with the overlying polar vortex through the breaking of primary GWs generated in the troposphere, or in an indirect way through interaction between the polar vortex and secondary GWs from the body force of breaking

© 2021. The Authors.

This is an open access article under the terms of the [Creative Commons Attribution-NonCommercial-NoDerivs License](https://creativecommons.org/licenses/by-nc-nd/4.0/), which permits use and distribution in any medium, provided the original work is properly cited, the use is non-commercial and no modifications or adaptations are made.

the primary GWs (Becker & Vadas, 2018; de Wit et al., 2017; Kogure et al., 2020; Liu et al., 2019; Preusse et al., 2002; Sato et al., 2009; Song et al., 2021).

The vertical propagation of GWs depends on the relationship given as a function of the horizontal phase velocity of GWs and background horizontal wind. When horizontal phase velocity vectors of GWs become close to a local horizontal wind vector as GWs propagate vertically, GW energies are absorbed in the mean flow and thus are filtered out, which is called “critical-level filtering” (Fritts & Alexander, 2003). This critical-level filtering is essential in understanding the spectral properties of GWs observed in the MLT region.

Spectral properties of small-scale GWs in the MLT such as wavelengths, phase speeds, and propagation directions can be directly observed in airglow layers using optical imagers. Taylor et al. (1993) investigated the properties of mesospheric short-period GWs (<1 hr) observed from airglow images and found that the propagation properties can be accounted for by critical-level filtering by background winds using blocking diagrams. The blocking diagram can illustrate spectral properties of upward propagating GWs that would not be detected at airglow altitudes. Traditionally, analysis of airglow images has been carried out in a subjective way that may vary depending on the personal preferences of researchers. To overcome the ambiguity of the subjective analysis, Matsuda et al. (2014) developed an objective analysis method (hereinafter, M-transform) to obtain power spectra as a function of the horizontal phase velocities from a sequence of normalized airglow intensity images. Using M-transform, Matsuda et al. (2017) successfully derived the characteristics of mesospheric GWs from all-sky imagers within Antarctic Gravity Wave Instrument Network (ANGWIN) that includes Syowa (69°S, 40°E), Halley (76°S, 27°W), Davis (69°S, 78°E), and McMurdo (78°S, 167°E) stations.

Kam et al. (2017) reported statistical distributions of individual wave structures in the airglow images at KSS using the traditional subjective analysis method. In this study, we investigate the spectral properties of upper mesospheric short-period GWs and their filtering by winds using airglow images observed at KSS over 5 years (2012–2016) by applying the M-transform method. Predominant propagating directions and spectral power of short-period GWs are derived using the M-transform method. Wind-blocking diagrams are constructed using the reanalysis wind data of the middle atmosphere and meteor radar wind data obtained at KSS. By comparing the propagation directions of observed GWs with wind-blocking diagrams, we demonstrate wind filtering effects on vertical propagation the GWs and discuss the fact that some of the GWs observed in the upper mesosphere can be generated in the upper stratosphere and lower mesosphere, not from the troposphere.

2. Data and Analysis

2.1. Airglow Image Observations

An all-sky camera (ASC) at KSS is manufactured by KEO Scientific Ltd. and has been operated by Korea Polar Research Institute (KOPRI) since 2008. The KSS ASC consists of a fish-eye-lens with a 180° field of view, the telecentric lens of two Plano-convex lenses, two narrow- and one wide-band interference filters, a multi-wavelength filter wheel (with OH Meinel bands, OI 557.7 nm, and OI 630.0 nm), and a 1024 × 1024 CCD with 2 × 2 binning. To avoid saturation on ASC images from luminous sources, the KSS ASC has been automatically operated when the solar elevation angle is less than −12°, and the lunar elevation angle is less than 0°. Detailed specifications of the instrument and basic image pre-processing methods are described in Kam et al. (2017).

Two of the three filters (OH Meinel bands, OI 557.7 nm, and OI 630.0 nm) installed on the ASC are mesospheric filters (OH Meinel bands of 720–910 nm around $z = 87$ km and OI 557.7 nm around $z = 95$ km). Investigation of the vertical propagating characteristics between two airglow emission heights for OH and OI 557.7 nm might be helpful to understand GW activities in the MLT region. However, in this study, we choose OH images to investigate the wind filtering effect of the middle atmosphere on the vertical propagation of mesospheric GWs. The OH filter has a wide bandwidth, so the OH images can have large intensity enough to capture alternating wave phases compared with OI 557.7 nm. The OH images have a mean spatial resolution of 1.17 km pixel^{−1} for entire images. The OH images are obtained with an exposure time of 20 s at a sampling interval of 328 s. This study utilizes OH images observed from 2012 to 2016, during which period the instrument has not been changed since the upgrade in 2012. Figure 1 shows seasonal distributions of the entire ASC operation time (gray) and operation time for the clear sky (blue) for the 5 years. Due to unfavorable weather conditions at KSS, the efficiency of observations used to analyze ASC images is about 4.45%, which corresponds to the ratio of the clear sky time of 392.78 hr to the total ASC operation time of 8822.82 hr for the 5-year period. In order to reduce potential sampling errors due to

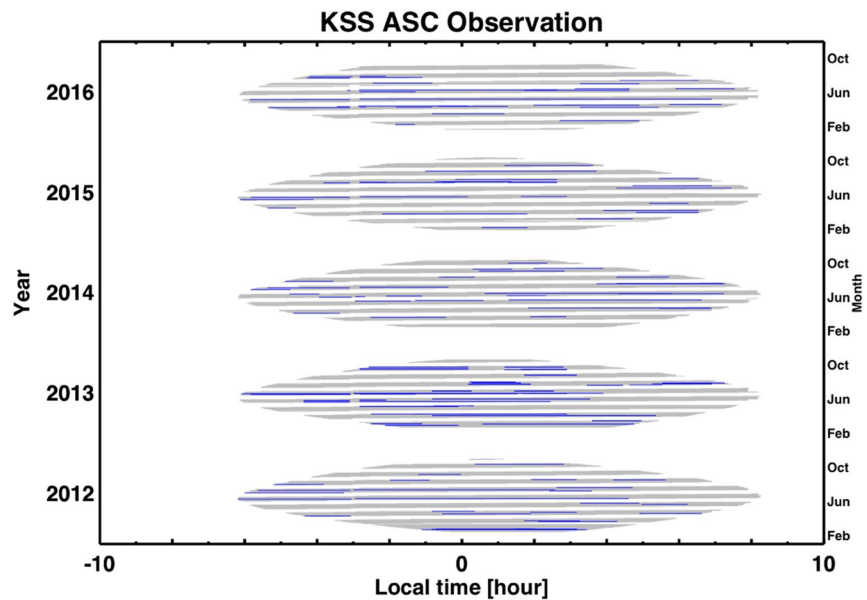


Figure 1. Time periods during which OH image observations are made at King Sejong Station (KSS) from 2012 to 2016. Lines plotted in gray and blue represent the entire operation time period and clear sky operation time period, respectively.

the use of relatively small amount of data, results are monthly averaged. Also, the sampling time periods in local time are quite random (Figure 1), and so sampling biases do not seem seriously large.

2.2. M-Transform

To investigate the spectral properties of mesospheric GWs, we employ M-transform, which was developed and released by National Institute Polar Research (Matsuda et al., 2014; Perwitasari et al., 2018) for the spectral analysis of the ASC image sequence. M-transform first computes the three-dimensional (3D) power spectral density (PSD) as a function of zonal and meridional wavenumbers (k and l) and frequency (ω) from the time sequence of the normalized horizontal images as I'/\bar{I} ($= (I - \bar{I})/\bar{I}$; I is the pixel intensity and \bar{I} is the temporally averaged intensity for the image sequence). At each frequency bin (ω), the 2D (k - l) section of the 3D PSD is converted to the phase-velocity PSD given as a function of phase speed (c) and propagation direction (ϕ). Then, the phase-velocity PSD obtained at each frequency bin is added for whole frequency bins, which yields the final airglow phase-velocity PSD as a function of c and ϕ . The phase-velocity PSD is normalized such that the integral of the 3D PSD with respect to k , l , and ω becomes identical to the integral of the phase-velocity PSD with respect to c and ϕ .

To calculate the phase velocity spectra, we set the ranges of wave parameters (horizontal wavelength, ground-based period, and ground-based phase speed) and sampling parameters (the size of horizontal square area and time period for analysis) according to Perwitasari et al. (2018). For the wave parameters, in this study, we choose 10–100 km for horizontal wavelengths, 15–60 min for ground-based wave periods, and 0–150 m s⁻¹ for observed phase speeds. For sampling parameters, we set the size of the horizontal square area for analysis to be larger than 150 × 150 pixels and smaller than the raw image size (512 × 512 pixels) to avoid clouds and galactic contamination due to the wideband nature of the OH filter. The time period for analysis (τ) is given by the number of consecutive clear sky images (N) [that is, $\tau = 328(N-1)$ s, where 328 s is the sampling time interval] illustrated in blue lines in Figure 1. The analysis is carried out only when τ is larger than 1 hr. The actual size of the horizontal area for analysis (larger than 150 × 150 pixels) and its location on the raw image are manually determined for individual clear sky events, but they are unchanged during each clear sky event.

For the spectral analysis for each clear sky event, 1024 and 256 bins are actually employed in each of the horizontal directions and in time, respectively. A series of the square horizontal pixel area for the time period (τ) is inserted in 1024² × 256 bins, and uninitialized bins are filled with zero values. Conventionally, GW studies based on ASC images have been carried out by analyzing specific images with clearly visible wave structures. In this

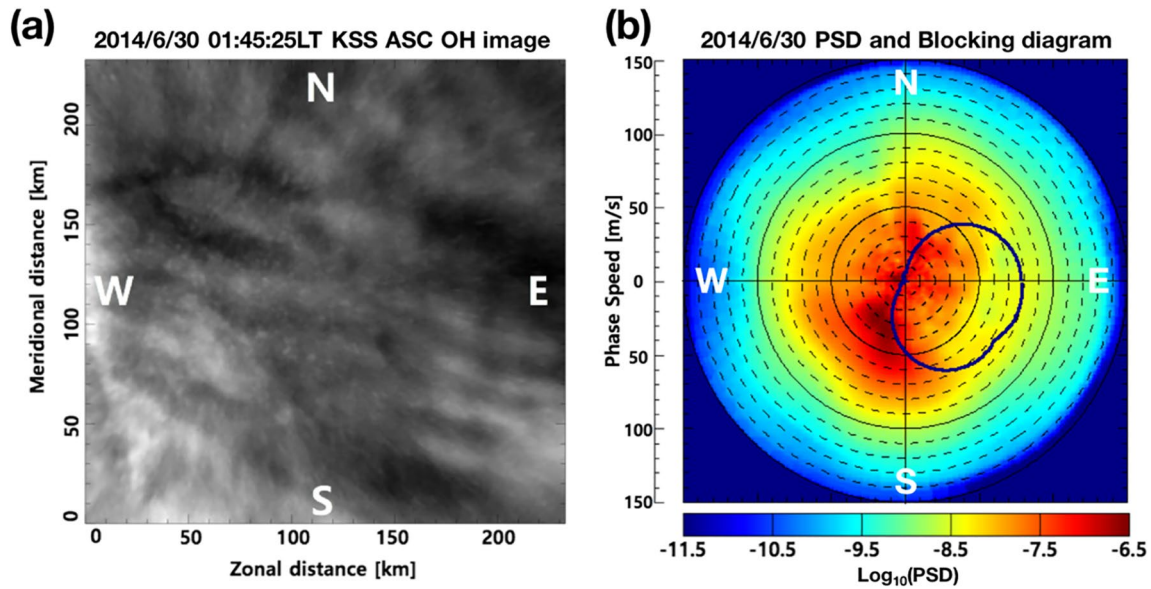


Figure 2. (a) An example of OH airglow image represented by (a) I'_{OH}/\bar{I}_{OH} at 01:45:25LT 30 June 2014 and (b) phase-velocity power spectral density (PSD) for a clear-sky event from 23:43:17LT 29 June to 04:46:55LT 30 June 2014). The navy line on Figure 2b represents a wind-blocking diagram.

study, however, we analyze all images in each clear-sky event without examining the existence of the visible wave structure. The total number of clear sky events used for the M-transform analysis is 107 for the 5-year period. Figures 2a and 2b show images of I'_{OH}/\bar{I}_{OH} observed on 30 June 2014 and its phase-velocity PSD, respectively. Predominant wave crests seem to be aligned in the NW-SE direction in Figure 2a, and the maximum powers are shown in the third quadrant (indicating SW propagation, consistent with the visible crests) with a speed range of 20–50 m s⁻¹ in Figure 2b.

2.3. Wind Data From KSS Meteor Radar and MERRA-2

To construct wind-blocking diagrams, stratospheric and mesospheric winds are obtained from the Modern-Era Retrospective analysis for Research and Applications, version-2 (MERRA-2) reanalysis dataset (Gelaro et al., 2017) and the meteor radar (MR) located at KSS. Since March 2007, KSS MR has been operated in all-sky interferometer mode with a peak power of 12 kW (8 kW before 2012) using the center frequency of 33.2 MHz. Details of the configurations of KSS MR and the wind extraction process from MR are described in Lee et al. (2013). In this study, we employ the hourly MR horizontal winds in the altitude range of 80–90 km. The MERRA-2 reanalysis dataset is produced by the NASA Global Modeling and Assimilation Office. We use the 3-hourly (00, 03, 06, 09, 12, 15, and 18 UTC) MERRA-2 provided with the horizontal resolution of $0.625^\circ \times 0.5^\circ$ and 74 vertical model levels from the ground to $z = 80$ km for this study. To obtain the MERRA-2 horizontal winds near KSS, the MERRA-2 winds are averaged over horizontal grid points around the location of KSS within $\pm 5^\circ$ in longitude and latitude.

A wind-blocking diagram is constructed using the method suggested by Taylor et al. (1993) where the horizontal-mean MERRA-2 winds and MR winds at KSS are averaged over the time period of a clear sky event. The diagram is defined by the boundaries of areas in the c - ϕ domain where the Doppler-shifted (intrinsic) frequency becomes negative for the observed ground-based phase speed and propagation direction of GWs with respect to a horizontal wind profile averaged over a clear sky event. The horizontal wind profile is determined by combining the horizontal wind profiles of MERRA-2 at altitudes of 0–80 km and MR winds at 80–90 km. The upper boundary of 90 km in the MR winds is chosen by considering the full-width at half maximum (8 km) of OH airglow layer around its center altitude of 86–87 km (Baker & Stair, 1988). An example wind-blocking diagram is over-plotted with a navy line in Figure 2b. Comparison between the diagram and phase-velocity PSD makes it possible to investigate the filtering effect, because the areas inside the blocking diagram are forbidden for GWs to propagate the airglow height from the lower atmosphere. In this study, in order to apply the wind-blocking diagram to the

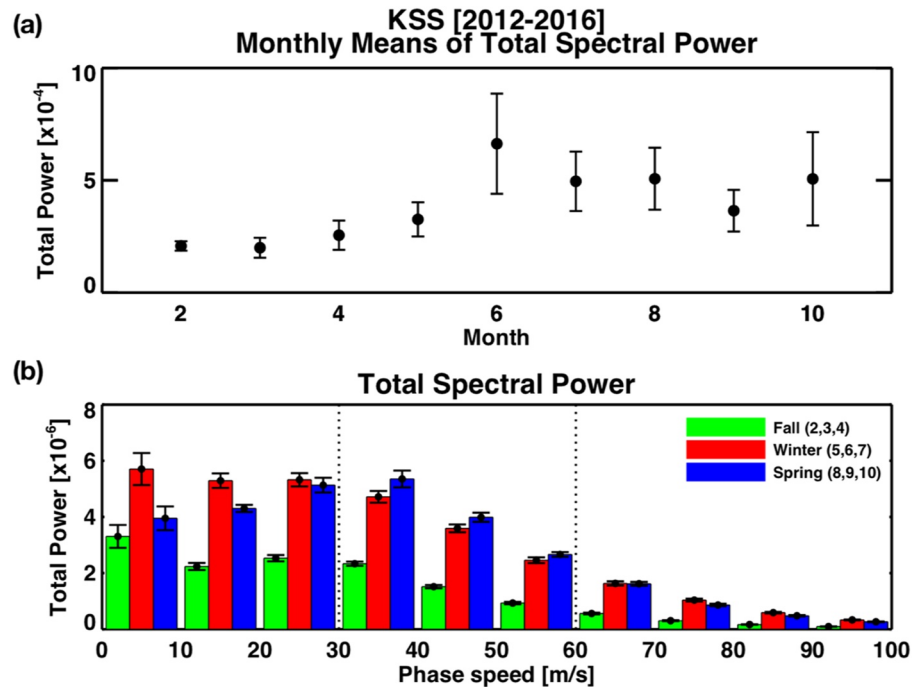


Figure 3. (a) Monthly means of total spectral powers (TSPs) (black dot) and their standard errors (error bars) of observed gravity waves (GWs) at King Sejong Station (KSS), and (b) histograms of TSPs as a function of phase speed for fall (green), winter (red), and spring (blue) with their standard errors (error bars). Note that the TSP in panel (b) is the same as the sum of $(I'/\bar{I})^2$ over all the propagation directions.

investigation of the wind filtering effect, we assume that the mesospheric GWs observed in the KSS ASC have propagated upward to $z = 90$ km in a vertical column with a horizontal plane of $\pm 5^\circ$ in longitude and latitude centered on the KSS. According to the results of the reverse ray trajectory method by Song et al., (2021), most of GWs observed in the KSS ASC were generated in this vertical volume, as shown in figure 9 in Song et al. (2021).

3. Results and Discussions

3.1. Seasonal Variations in Short-Period GW Activity

The total spectral power (TSP) is calculated by integrating the two-dimensional PSDs (e.g., the PSD shown in Figure 2b) obtained for individual clear-sky events with respect to phase speed (c) and propagation direction (ϕ). In this section, the TSP is used as an index to represent the activity of the short-period (< 1 hr) GWs.

Seasonal variations of GW activities are examined by calculating monthly averaged TSPs. The number of clear-sky events used for monthly averaging in each month increases from summer to winter and ranges from 7 to 16 between February and October. Small values (7–8) occur in February and October, but large values (15–16) are found in June, July, and August. Figure 3a shows the monthly mean TSP averaged over the whole observational period of 5 years from 2012 to 2016. The largest GW activity occurs in Austral winter (June), as noted in the previous study (Table 1 in Kam et al., 2017), and moderate GW activities are retained from late winter to spring (August–October). The standard error of the monthly mean TSPs is also the largest in June, implying high variability of GW activities in winter. Previous studies on GWs over the Antarctic Peninsula have reported large GW activities during winter in the mesosphere (Espy et al., 2006), the stratosphere (Baumgaertner & McDonald, 2007; Hoffmann et al., 2013, 2017; Jiang et al., 2003), and the thermosphere (Park et al., 2014). These similar seasonal characteristics of GW activities from the stratosphere to the thermosphere suggests that observed short-period GWs in OH airglow images can be upward propagating GWs generated from well-known typical sources such as mountains over the Antarctic Peninsula and vigorous tropospheric or stratospheric jet systems over the Southern Ocean. However, the observed GW activities in the upper atmosphere may not only be accounted for by the tropospheric (or stratospheric) primary sources but also involve secondary GW generation after the breaking of the

primary GWs from the lower atmosphere on their way to the upper atmosphere. Recently, using a high-resolution global circulation model, Becker and Vadas (2018) suggested that secondary GWs can be generated during winter from the body force of breaking primary waves in the stratosphere and lower mesosphere around 60° S. Kogure et al. (2020) supported this secondary generation mechanism by satellite observations. They observed partial concentric GWs in the OH layer over the southern ocean and demonstrated that those GWs were secondary gravity waves created by mountain wave breaking.

Before the propagation directions of observed GWs are investigated in terms of wind filtering, the phase speed distribution obtained from the M-transform analysis is examined (Figure 3b). Here, the phase speed represents the horizontal propagation speed of GWs detected in the sequence of observed images. The observed waves predominantly have slow-to-moderate phase speeds ($<60 \text{ m s}^{-1}$). To investigate the seasonal variations of phase speeds, we divided the observed GWs into three groups according to their phase speeds: Slow GWs at 0–30 m s^{-1} , moderately fast GWs at 30–60 m s^{-1} , and fast GWs higher than 60 m s^{-1} . The slow, moderately fast, and fast waves are 52%, 37%, and 11% of all the observed GWs, respectively. Slow GWs are dominant in winter and spring, but interestingly, moderately fast GWs with phase speeds of 30–60 m s^{-1} are more pronounced in spring. The enhancement of the moderately fast GWs in spring seems related to the faster horizontal propagation of GWs generated from the lower stratospheric jets in the transition period from winter to spring compared with the winter period, which was demonstrated by Murphy et al. (2014) using 12-year radiosonde observations made at the Davis station, Antarctica (see their figure 11 for details).

3.2. Evidence of the Wind Filtering Effect

Figure 4 shows the monthly averaged PSDs averaged over three phase-speed ranges (0–30, 30–60, and 60–100 m s^{-1}) (Figures 4a–4c) and monthly normalized PSDs for better illustration of wind-blocking (Figures 4d–4f) as a function of the months and azimuthal angles for slowly, moderately fast and fast propagating GWs. The monthly averaged values of the magnitudes of phase speeds (for given azimuth angles) at the boundaries of wind-blocking diagrams calculated with wind profiles from 50 to 90 km and from 10 to 90 km are overplotted with purple solid and navy dashed contours, respectively. Upward propagating GWs, generated from the troposphere or stratosphere, with phase speeds smaller than the numbers on contour lines encounter the critical layer where the phase speed is equal to the background wind, and thus are not expected to propagate up to the mesospheric OH airglow layer that the ASC observes. On the other hand, GWs with phase speeds higher than the numbers on contour lines do not meet the critical layer, and therefore are not filtered out.

It is evident from Figures 4a and 4d that the structure of the PSDs for the slowly propagating GWs is clearly explained by the wind-blocking contours [for example, the dominance of westward propagating GWs in winter (May, June, and July) and lack of westward propagating GWs in fall (February and March) and spring (October)]. The monthly mean PSDs of moderately fast propagating GWs (Figures 4b and 4e) are also fairly well accounted for by the wind-blocking contours, with the exception of some of the southeastward propagating GWs in October. Meanwhile, the monthly averaged PSDs of the fast propagating GWs (Figures 4c and 4f) are quite uncorrelated with the wind-blocking contours, especially in winter. The fast propagating GWs are not expected to be blocked by tropospheric or stratospheric winds because they propagate faster than the maximum winds in the middle atmosphere below the stratopause. In short, Figure 4 provides features of wind-blocking effects in the observed mesospheric GWs in a qualitative sense.

Comparison of GW propagation directions obtained from airglow images with wind-blocking diagrams has been reported for particular GW events observed in a relatively short period of time (Essien et al., 2018; Medeiros et al., 2003; Taylor et al., 1993). In contrast, the diagram shown in Figure 4 in the present study provides climatological and seasonal views of wind filtering effects on the propagation direction of GWs observed from the ASC. The predominance of the westward propagating mesospheric GWs in winter has also been reported from imaging observations near KSS in the Antarctic Peninsula, such as Rothera station (67°S, 68°W) (Espy et al., 2006) and Comandante Ferraz station (62°S, 58°W) (Bageston et al., 2009). It is widely accepted that the predominance of westward propagating GWs in winter is due to the strong eastward stratospheric polar jet that filters out the eastward propagating GWs generated in the troposphere and lower stratosphere. However, the reason for propagation directions in fall and spring (lack of westward propagation and enhancement of southeastward propagation) has not been examined in the Antarctic Peninsula region.

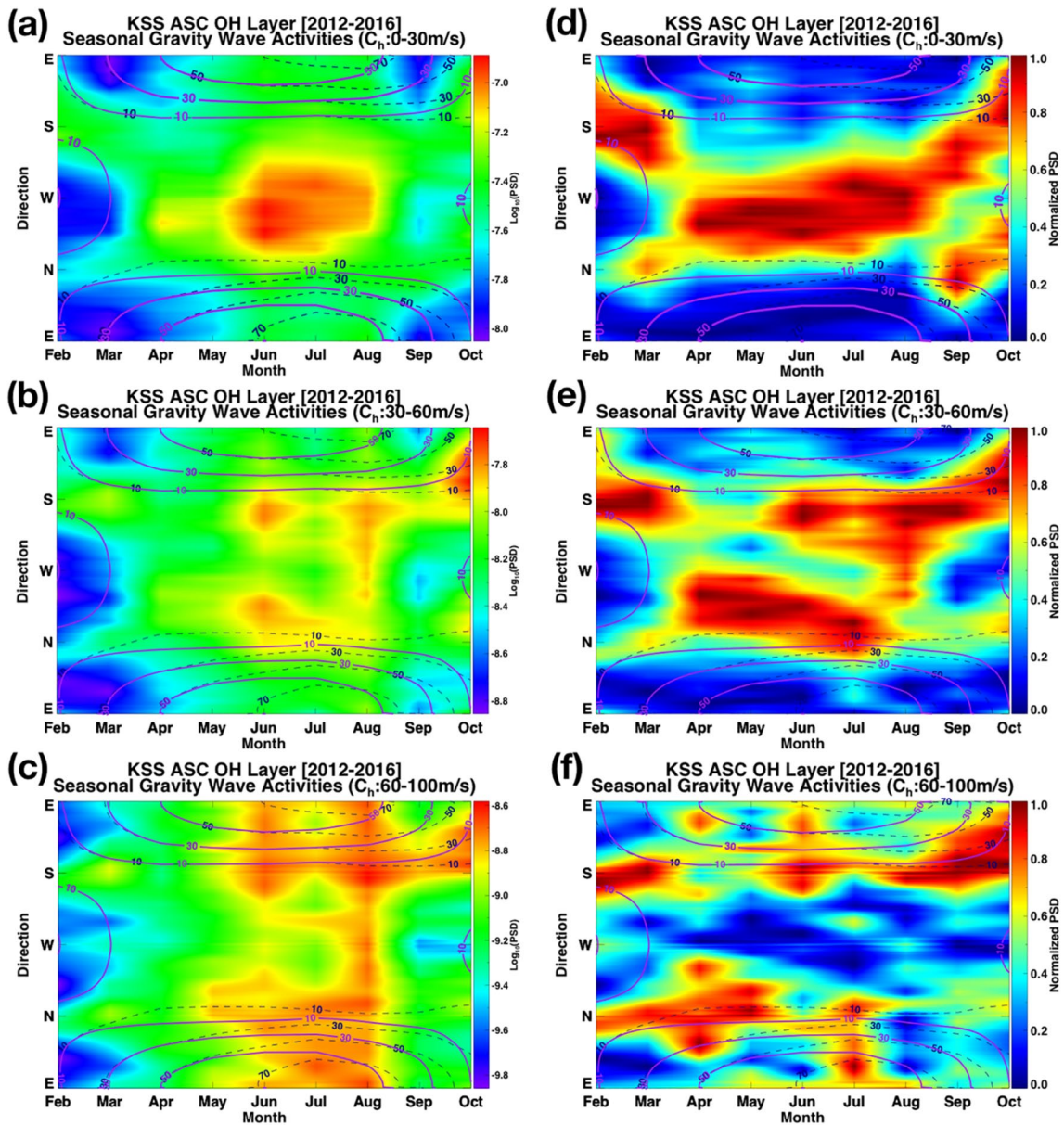


Figure 4. Monthly mean power spectral densities (PSDs) of gravity waves (GWs) averaged over three horizontal phase-speed ranges of (a) 0–30 m s⁻¹, (b) 30–60 m s⁻¹, and (c) 60–100 m s⁻¹ in the month and propagation direction domain. The monthly mean PSDs are calculated from the 5-year (2012–2016) observations. Panels (d), (e), and (f) show the monthly normalized forms of the PSDs shown in (a), (b), and (c), respectively, to provide a better illustration of wind blocking. The monthly normalization is performed by making the magnitudes of the PSDs range between zero to one for each month.

3.3. GWs of Middle Atmospheric Origin

The wind-blocking diagrams can explain the overall structure of the two-dimensional (c – ϕ) PSDs of the observed mesospheric GWs, but they cannot for some propagation directions and altitude ranges in particular seasons. Concerning incongruent features between PSD and blocking diagram, southeastward propagating GWs in October are interesting, Figure 4a shows the slowly propagating southeastward large-amplitude GWs in October. The PSDs for these southeastward GWs are overlapped by the 30 m s⁻¹ wind-blocking contours (with navy dashed contours) calculated using wind profiles from 10 to 90 km, but they are not overlapped by wind-blocking contours obtained from wind profiles from 50 to 90 km (with purple solid contours). This result indicates that the slowly southeastward propagating GWs can propagate upward without being filtered in the mesosphere above the altitude of 50 km. Of course, the components of unfiltered GWs could include the possibility of observing GWs in

the KSS ASC that have propagated horizontally over long distance and then penetrated above the mesosphere in the vertical columns. However, as mentioned above, we assumed that the GWs observed in the ASC propagated through the vertical column over KSS based on the results of Song et al. (2021). Similar to slowly propagating GWs, southeastward propagating GWs in October are also found in the moderately fast and fast propagating GW groups (see Figures 4b–4c and 4e–4f). These southeastward propagating GWs in all the three phase-speed groups may potentially be generated from the same source in the mesosphere.

In order to check the extent to which the upper mesospheric GWs observed by the ASC can be generated in the troposphere, the stratosphere, or the lower mesosphere, various blocking diagrams calculated using wind profiles with different lower boundaries are compared with a PSD obtained on a specific date (5 October 2013), and they are illustrated in Figure 5. Lower boundaries (H_{low}) of wind profiles used in the blocking diagrams range from the surface to the altitude of 80 km at an interval of 10 km. Using a given PSD and blocking diagrams, the vertical propagation efficiency is calculated for each blocking diagram and plotted in each panel of Figure 5. The propagation efficiency is defined by the ratio of the sum of the spectral powers unblocked by the filtering diagrams to the total spectral powers of the PSD, where $\overline{P_{bd}}$ (written in Figure 5) is the mean value of the spectral powers on blocking diagram. When $\overline{P_{bd}}$ has a smaller value, it means the blocking diagram well describes an effective wind filtering in PSD.

The PSD shown in Figure 5 indicates the predominance of the southeastward propagating GWs with the phase speeds of 30–55 m s⁻¹ at the airglow height. For $H_{low} \leq 40$ km, the wind-blocking areas are too broad to explain the smallness of the PSD in the phase speeds less than 30 m s⁻¹ in the southeastward direction. A significant activity of the southeastward propagating GW is seen inside the blocking diagram for $H_{low} \leq 40$ km, and the propagation efficiency is generally as low as 58%. For $H_{low} \geq 50$ km, however, the wind-blocking areas are substantially congruent with the spectral areas of the small-amplitude PSD. Compared with $H_{low} \leq 40$ km, the size of the diagram is reduced, and the propagation efficiency jumps up to about 95% around 50 km. If the southeastward propagating large-amplitude GWs originate from the troposphere and stratosphere, they should have been substantially blocked by the stratospheric winds. However, in terms of the incongruent PSD feature with the diagrams for $H_{low} \leq 40$ km, the filtering effect by the stratospheric winds is not found in the PSD, and it cannot explain the southeastward propagating GWs are originated below 40 km. Therefore, it looks probable that the observed southeastward propagating GWs started around and above 50 km, at least on that particular night (5 October 2013). This result suggests the possibility of the mesospheric origin of those GWs.

The possibility of the mesospheric origin of GWs is checked for all clear sky events. Figure 6 shows the histogram for the lower boundaries of wind profiles that give the minimum $\overline{P_{bd}}$ ($H_{low-min}$) and the vertical propagation efficiency as a function of month and H_{low} . For each clear sky event, $\overline{P_{bd}}$ (the mean spectral power on the wind-blocking diagrams) is evaluated for nine different values of H_{low} (0–80 km at an interval of 10 km), and the minimum $\overline{P_{bd}}$ denotes the minimum value among the nine values of $\overline{P_{bd}}$. The H_{low} where the minimum $\overline{P_{bd}}$ is found is denoted by $H_{low-min}$. When same $\overline{P_{bd}}$ s and blocking diagram regardless of changing H_{low} in a specific height range, we adopted the minimum height in the range to define $H_{low-min}$. All GWs unfiltered by the wind-blocking diagrams are not generally vertically propagating, but most of the observed GWs satisfy the vertical propagation condition ($m^2 > 0$, where m is the vertical wavenumber of a GW packet) in the spectral domain of the two-dimensional PSDs computed from the M-transform method (not shown). In fact, the spectral powers in the vertically propagating spectral domain where $m^2 > 0$ are about 10³ times larger than those in the evanescent spectral domain where $m^2 \leq 0$.

With respect to the physical meaning of the $H_{low-min}$, note that GWs observed in the airglow height around 90 km in each clear-sky event can most probably be generated in any of the altitudes between $H_{low-min}$ and 90 km. For example, the fact that the $H_{low-min}$ of 0 km is found in 32.42% of clear sky events indicates that the source of GWs observed near 90 km can be located between 0 and 90 km for 32.42% of clear sky events. On the other hand, Figure 6a also indicates that the source of GWs observed in the airglow height near 90 km cannot be explained below 20 km for 58.32 (12.04 + 8.33 + 14.81 + 14.81 + 8.33)% combined by the portions for $H_{low-min}$ range from 20 to 80 km. In other words, at a minimum, the proportion of 58.32% of the events indicates that about half or more of the GWs observed from the airglow images might be generated above the middle atmosphere, such as in the stratosphere and mesosphere, not from the troposphere. Likewise, it can be seen from Figure 6a that the probability of attributing GWs observed at the airglow height to sources located at the MLT region can be as high as 23.14 (14.81 + 8.33)%. Given that there is the possibility of the generation of GWs from the ground for only 32.42% of

2013/10/5 PSD and Blocking diagrams

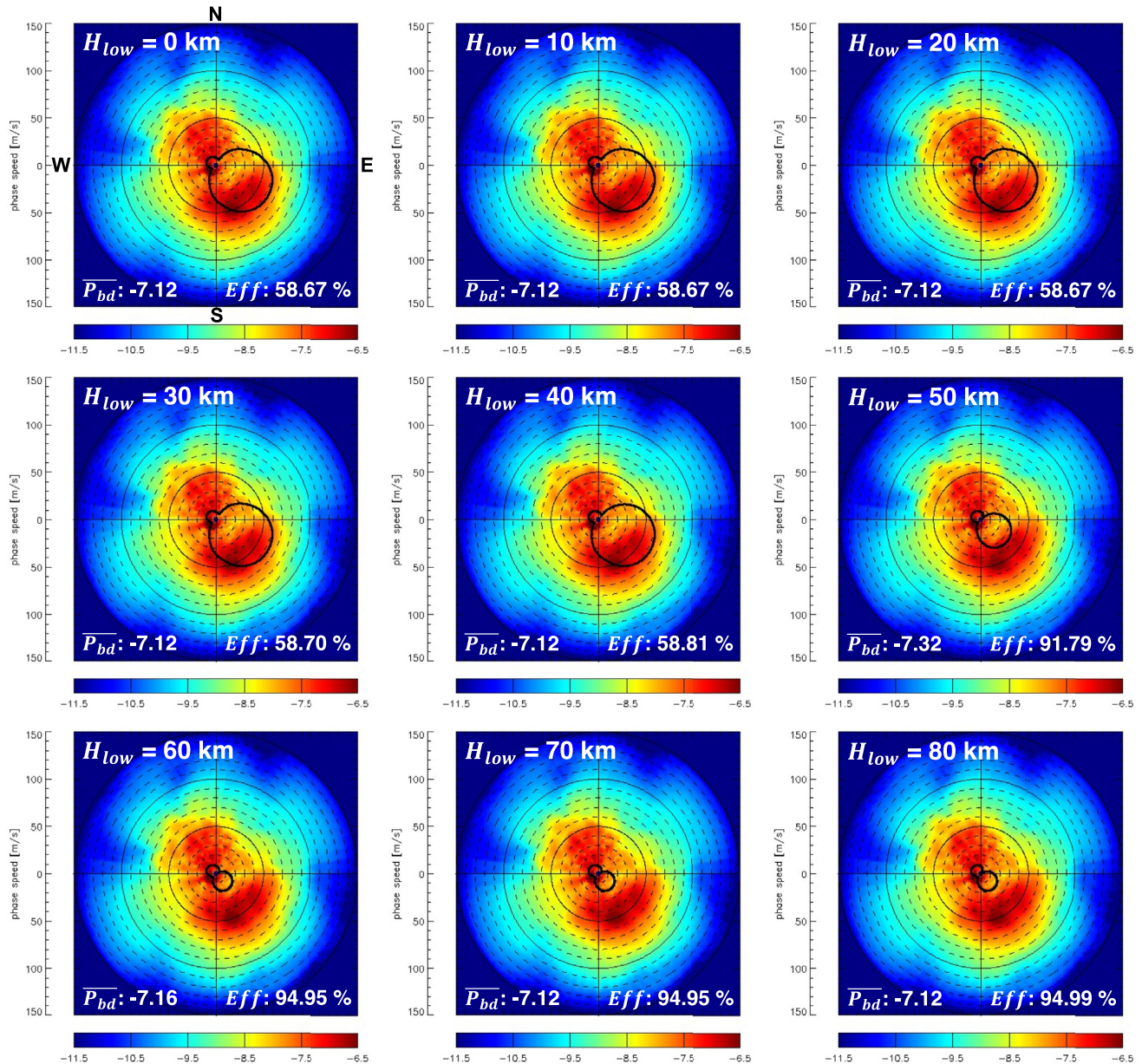


Figure 5. A two-dimensional power spectral density (PSD) (shading) of the gravity waves (GWs) observed at night on 5 October 2013 and wind-blocking diagrams (thick contours) constructed using wind profiles from various lower boundaries ($H_{low} = 0\text{--}80$ km at an interval of 10 km) to 90 km. \overline{P}_{bd} represents the logarithmic value of the mean of the spectral powers on the areas of the blocking diagrams. The vertical propagation efficiency (Eff) is defined by the ratio of the spectral powers outside of the blocking diagrams to the total spectral power.

clear sky events, it is clear that a substantial amount of observed mesospheric GWs near 90 km over KSS can possibly be generated in the middle atmosphere. Note that the $H_{low-min}$ does not depend on the wind structure alone. The $H_{low-min}$ is determined by examining consistency between the PSD of the GWs observed in the airglow height and the wind-blocking diagrams calculated from the nine overlapping layers below the observation altitude.

In addition to the estimation of the potential source layer of the GWs observed in the airglow height based on the 5-year averaged vertical propagation properties, seasonal variations of the vertical propagation efficiency are examined (Figure 6b). As is expected from the definition of propagation efficiency, the efficiency generally increases as the H_{low} approaches the airglow height (90 km). The $H_{low-min}$ is the altitude of the lower boundary of

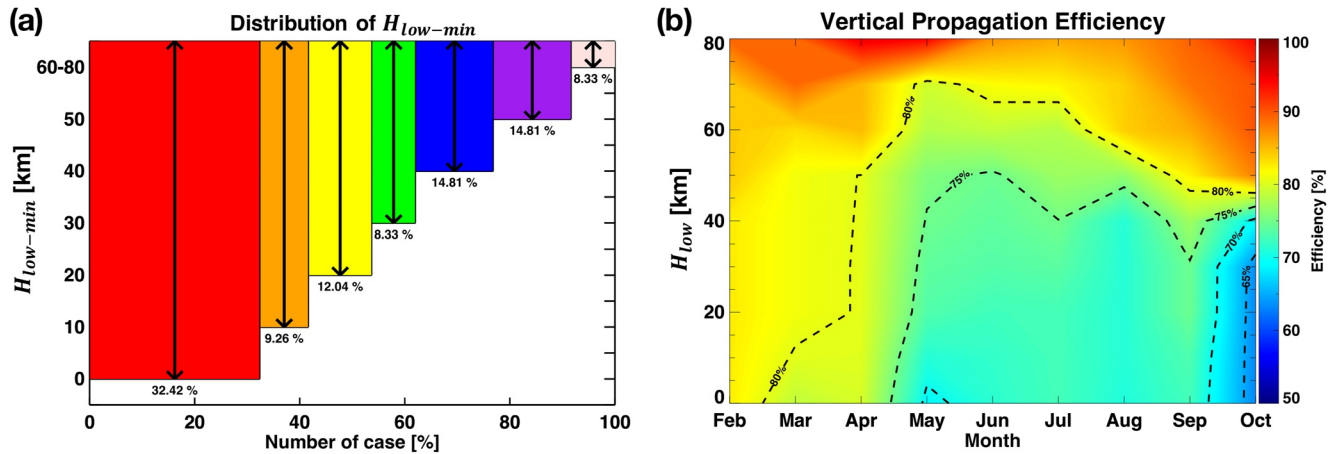


Figure 6. (a) The histogram of the $H_{low-min}$ for all the clear sky events, and (b) seasonal variation of the vertical propagation efficiency as a function of month and H_{low} . The $H_{low-min}$ in panel (a) denotes the lower boundaries of wind profiles that give the minimum $\overline{P_{bd}}$.

the most probable source region for GWs observed at 90 km, and the propagation efficiency is found to generally range from 75% to 80% at $H_{low-min}$ (not shown). This result indicates that the lower boundary of the source region for GWs at the airglow height exhibits a clear seasonal variation, which is confirmed by the contour lines of 75% and 80% shown in Figure 6b. In other words, the vertical regions above the 75%–80% contour lines (shaded in yellow and red) indicate the potential source regions for the GWs observed at 90 km.

The wind-blocking diagrams are calculated from wind profiles. Therefore, the vertical propagation efficiency depends on the seasonal variations of the wind profiles, although the efficiency is not solely determined by wind structure because it involves how much the spectral powers are blocked or unblocked. In fall (February, March, and April), it is probable that the observed GWs can propagate directly from the surface, due to relatively weak wind and small wind shear compared with the other seasons. In fact, the propagation efficiency is over 80% throughout the entire height range. Meanwhile, in winter and spring (June to October) when the Antarctic stratospheric polar vortex is strong (Zuev & Savelieva, 2019), the structure of the PSDs (see Figures 4a and 4b) is not clearly accounted for by the blocking diagrams that include lower stratospheric winds. In addition, in winter and spring, the magnitudes of the propagation efficiencies are less than 75% below the upper stratosphere or the lower mesosphere. This result indicates that GWs generated from the troposphere or stratosphere in austral winter and spring can be filtered out by the robust polar stratospheric winds, and GWs observed at the winter and spring airglow height may be generated above the upper stratosphere or lower mesosphere.

In addition to the southeastward propagating GWs in October, there are additional GWs for which PSD cannot be sufficiently explained by the wind blocking diagrams, and they are eastward propagating GWs with moderately large amplitudes in winter (see Figures 4a and 4b). The eastward propagating GWs in winter have logarithmic PSD powers larger than -7.5 (-8.2) for $c = 0-30$ m s^{-1} ($30-50$ m s^{-1}). In winter, eastward propagating GWs generated from the troposphere can be substantially blocked by the strong eastward jet in the stratosphere. Since the austral eastward winter jet is robust, the eastward propagating GWs observed at the airglow height in winter can be of mesospheric origin. Furthermore, individual winter PSDs, as shown in Figures 2b and 4, and Text S1 in Supporting Information S1, exhibit less anisotropy compared with the other seasons. These reduced anisotropies in winter PSD can be attributed to secondary GWs according to Vadas et al. (2003), who proposed that secondary GWs generated from the body force of breaking primary GWs can propagate in all directions. Becker and Vadas (2018) demonstrated using the high-resolution model simulations that the secondary waves can be generated during winter from the body force of the breaking primary waves in the stratosphere and lower mesosphere around 60°S. Therefore, the eastward propagating GWs observed in winter can originate from the breaking of primary waves in the stratosphere. In addition, according to de Wit et al. (2017), at the lee of the Southern Andes (54°S) in winter, the large eastward GW momentum fluxes at MLT region estimated from MR cannot be explained by the upward propagating GWs through the eastward stratospheric jet, so their unexpected results are interpreted as secondary GWs.

Alternatively, the eastward propagating GWs may be of tropospheric origin from distant regions. Kogure et al. (2018) observed an enhancement of GW energy over Syowa in August, and attributed this to GW refraction from various latitudes. In the present study, however, the possibility of long-range propagation of GWs observed at the airglow height is not examined. For proper understanding, ray-tracing approaches as in Song et al. (2020), which was outside of the scope of this study, might be required. Matsuda et al. (2017) compared individual PSDs with the blocking diagrams over Syowa, Halley, and McMurdo, and found the effect of wind filtering. They also noted the discrepancy between wave propagation directions and wind-blocking diagrams over Davis, and speculated that it might be due to secondary GWs above the stratosphere. Applying a backward ray-tracing analysis of GWs observed at the KSS ASC (Song et al., 2021), a number of the observed GW events were terminated in the mesosphere and they were considered as secondary GWs, which might be associated with the breaking of orographic primary GWs of reaching the lower mesosphere, especially in winter.

4. Summary and Conclusions

In the present study, we analyzed all-sky OH airglow images observed at KSS for 5 years (2012–2016) using the M-transform method. The M-transform of the OH images results in the two-dimensional PSD of a short period (<1 hr) GWs as a function of phase speeds and propagation directions. The magnitude and propagation directions of GWs show clear seasonal variation, with strong activities in mid-winter. To understand the seasonal variations in the horizontal propagation of mesospheric GWs, we constructed climatological wind-blocking diagrams from MERRA-2 (0–80 km) and KSS MR (80–90 km) wind data. The predominant directions of observed waves with slow speeds (0–30 m s⁻¹) are clearly anti-correlated with wind-blocking directions, providing graphical evidence of wind filtering effects on mesospheric waves observed with KSS ASC. However, we also found moderately strong eastward wave activities in winter despite the strong eastward wind blocking in the middle atmosphere. The less anisotropic nature of GWs in winter, due to the moderate eastward propagating GWs, is consistent with the secondary wave theory. The secondary waves are believed to be generated from the breaking of primary waves in the middle atmosphere. We also noted that strong southeastward propagating GWs in spring might be generated above the altitude of 50 km inferred from the spectral powers on the blocking diagram.

Data Availability Statement

The observation data as the meteor radar and all-sky airglow images at King Sejong Station are available from Korea Polar Data Center (KPDC) (<https://kpsc.kopri.re.kr/>). M-transform software was provided from the National Institute of Polar Research (<http://polaris.nipr.ac.jp/~airglow/M-transform/>) and MERRA-2 data were downloaded from NASA Global Modeling and Assimilation Office (<http://gmao.gsfc.nasa.gov/reanalysis/MERRA-2/>).

Acknowledgments

This research was supported by basic research funding from the Korea Astronomy and Space Science Institute (KASI) (KASI2021185005) and by a National Research Foundation of Korea (NRF) grant funded by the Korean government (MSIT) (2019K2A9A1A0610292012). This work was also supported by grant PE21020 from the Korea Polar Research Institute and studied as a part of collaboration work in the ANGWIN community. M. K. was supported by the JSPS grant JRP-LEAD with DFG program, JSPS KAKENHI 19K23465 and the Scientific Committee on Antarctic Research (SCAR) fellowship award 2019.

References

- Alexander, M. J., & Teitelbaum, H. (2007). Observation and analysis of a large amplitude mountain wave event over the Antarctic peninsula. *Journal of Geophysical Research: Atmosphere*, *112*, D21103. <https://doi.org/10.1029/2006JD008368>
- Bageston, J. V., Wrasse, C. M., Gobbi, D., Takahashi, H., & Souza, P. B. (2009). Observation of mesospheric gravity waves at Comandante Ferraz Antarctica station (62°S). *Annales Geophysicae*, *27*, 2593–2598. <https://doi.org/10.5194/angeo-27-2593-2009>
- Baker, D. J., & Stair, A. T., Jr. (1988). Rocket measurements of the altitude distributions of the hydroxyl airglow. *Physica Scripta*, *37*, 611–622. <https://doi.org/10.1088/0031-8949/37/4/021>
- Baumgaertner, A. J. G., & McDonald, A. J. (2007). A gravity wave climatology for Antarctica compiled from Challenging Minisatellite Payload/Global Positioning System (CHAMP/GPS) radio occultations. *Journal of Geophysical Research: Atmosphere*, *112*(D5), D05103. <https://doi.org/10.1029/2006JD007504>
- Becker, E. (2012). Dynamical control of the middle atmosphere. *Space Science Reviews*, *168*, 238–314. <https://doi.org/10.1007/s11214-011-9841-5>
- Becker, E., & Vadas, S. L. (2018). Secondary gravity waves in the winter mesosphere: Results from a high-resolution global circulation model. *Journal of Geophysical Research: Atmosphere*, *123*, 2605–2627. <https://doi.org/10.1002/2017JD027460>
- de Wit, R. J., Janches, D., Fritts, D. C., Stockwell, R. G., & Coy, L. (2017). Unexpected climatological behavior of MLT gravity wave momentum flux in the lee of the Southern Andes hot spot. *Geophysical Research Letters*, *44*, 1182–1191. <https://doi.org/10.1002/2016GL072311>
- Ern, M., Preusse, P., Alexander, M. J., & Warner, C. D. (2004). Absolute values of gravity wave momentum flux derived from satellite data. *Journal of Geophysical Research: Atmosphere*, *109*, D20103. <https://doi.org/10.1029/2004JD004752>
- Espy, P. J., Hibbins, R. E., Swenson, G. R., Tang, J., Taylor, M. J., Riggins, D. M., & Fritts, D. C. (2006). Regional variations of mesospheric gravity-wave momentum flux over Antarctica. *Annales Geophysicae*, *24*, 81–88. <https://doi.org/10.5194/angeo-24-81-2006>
- Essien, P., Paulino, I., Wrasse, C. M., Campos, J. A. V., Paulino, A. R., Medeiros, A. F., et al. (2018). Seasonal characteristics of small- and medium-scale gravity waves in the mesosphere and lower thermosphere over Brazilian equatorial region. *Annales Geophysicae*, *36*, 899–914. <https://doi.org/10.5194/angeo-36-899-2018>
- Fritts, D. C., & Alexander, M. J. (2003). Gravity wave dynamics and effects in the middle atmosphere. *Reviews of Geophysics*, *41*(1), 1003. <https://doi.org/10.1029/2001RG000106>

- Gelaro, R., McCarty, W., Suárez, M. J., Todling, R., Molod, A., Takacs, L., et al. (2017). The Modern-Era retrospective analysis for reanalysis and Applications, version 2 (MERRA-2). *Journal of Climate*, *30*(14), 5419–5454. <https://doi.org/10.1175/jcli-d-16-0758.1>
- Hindley, N. P., Wright, C. J., Smith, N. D., & Mitchell, N. J. (2015). The southern stratospheric gravity wave hot spot: Individual waves and their momentum fluxes measured by COSMIC GPS-RO. *Atmospheric Chemistry and Physics*, *15*, 7797–7818. <https://doi.org/10.5194/acp-15-7797-2015>
- Hoffmann, L., Spang, R., Orr, A., Alexander, M. J., Holt, L. A., & Stein, O. (2017). A decadal satellite record of gravity wave activity in the lower stratosphere to study polar stratospheric cloud formation. *Atmospheric Chemistry and Physics*, *17*, 2901–2920. <https://doi.org/10.5194/acp-17-2901-2017>
- Hoffmann, L., Xue, X., & Alexander, M. J. (2013). A global view of stratospheric gravity wave hotspots located with Atmospheric Infrared Sounder Observation. *Journal of Geophysical Research: Atmosphere*, *118*(2), 416–434. <https://doi.org/10.1029/2012JD018658>
- Jiang, J. H., Wu, D. L., Eckermann, S. D., & Ma, J. (2003). Mountain waves in the middle atmosphere: Microwave Limb Sounder observations and analyses. *Advances in Space Research*, *32*(5), 801–806. [https://doi.org/10.1016/S0273-1177\(03\)00402-2](https://doi.org/10.1016/S0273-1177(03)00402-2)
- Kam, H., Jee, G., Kim, Y. H., Ham, Y.-b., & Song, I.-S. (2017). Statistical analysis of mesospheric gravity waves over King Sejong Station, Antarctica (62.2°S, 58.8°W). *Journal of Atmospheric and Solar-Terrestrial Physics*, *155*, 86–94. <https://doi.org/10.1016/j.jastp.2017.02.006>
- Kim, Y.-J., Eckermann, S. D., Chun, H.-Y., & Chun, H. Y. (2003). An overview of the past, present, and future of gravity-wave drag parameterization for numerical climate and weather prediction models. *Atmosphere-Ocean*, *41*, 65–98. <https://doi.org/10.3137/ao.410105>
- Kogure, M., Nakamura, T., Ejiri, M. K., Nishiyama, T., Tomikawa, Y., & Tsutsumi, M. (2018). Effects of horizontal wind structure on a gravity wave event in the middle atmosphere over Syowa (69°S, 40°E), the Antarctic. *Geophysical Research Letters*, *45*, 5151–5157. <https://doi.org/10.1029/2018GL078264>
- Kogure, M., Yue, J., & Liu, H. (2021). Gravity wave weakening during the 2019 Antarctic stratospheric sudden warming. *Geophysical Research Letters*, *48*, e2021GL092537. <https://doi.org/10.1029/2021GL092537>
- Kogure, M., Yue, J., Nakamura, T., Hoffmann, L., Vadas, S. L., Tomikawa, Y., et al. (2020). First direct observational evidence for secondary gravity waves generated by mountain waves over the Andes. *Geophysical Research Letters*, *47*, e2020GL088845. <https://doi.org/10.1029/2020GL088845>
- Lee, C., Kim, Y. H., Jee, G., Kim, J.-H., Won, Y.-I., & Wu, D. L. (2013). Seasonal variation of wave activities near the mesopause region observed at King Sejong Station (62.22°S, 58.78°W), Antarctica. *Journal of Atmospheric and Solar-Terrestrial Physics*, *105–106*, 30–38. <https://doi.org/10.1016/j.jastp.2013.07.006>
- Lindzen, R. S. (1981). Turbulence and stress owing to gravity wave and tidal breakdown. *Journal of Geophysical Research: Oceans*, *86*(C10), 9707–9714. <https://doi.org/10.1029/jc086ic10p09707>
- Liu, X., Xu, J., Yue, J., Vadas, S. L., & Becker, E. (2019). Orographic primary and secondary gravity waves in the middle atmosphere from 16-year SABER observations. *Geophysical Research Letters*, *46*, 4512–4522. <https://doi.org/10.1029/2019GL082256>
- Matsuda, T. S., Nakamura, T., Ejiri, M. K., Tsutsumi, M., & Shiokawa, K. (2014). New statistical analysis of the horizontal phase velocity distribution of gravity waves observed by airglow imaging. *Journal of Geophysical Research: Atmosphere*, *119*(16), 9707–9718. <https://doi.org/10.1002/2014JD021543>
- Matsuda, T. S., Nakamura, T., Ejiri, M. K., Tsutsumi, M., Tomikawa, Y., Taylor, M. J., et al. (2017). Characteristics of mesospheric gravity waves over Antarctica observed by Antarctic Gravity Wave Instrument Network imagers using 3-D spectral analyses. *Journal of Geophysical Research: Atmosphere*, *122*, 8969–8981. <https://doi.org/10.1002/2016JD026217>
- Medeiros, A. F., Taylor, M. J., Takahashi, H., Batista, P. P., & Gobbi, D. (2003). An investigation of gravity wave activity in the low-latitude upper mesosphere: Propagation direction and wind filtering. *Journal of Geophysical Research: Atmosphere*, *108*(D14), 4411. <https://doi.org/10.1029/2002jd002593>
- Murphy, D. J., Alexander, S. P., Klekociuk, A. R., Love, P. T., & Vincent, R. A. (2014). Radiosonde observations of gravity waves in the lower stratosphere over Davis, Antarctica. *Journal of Geophysical Research: Atmosphere*, *119*(21), 11973–11996. <https://doi.org/10.1002/2014jd022448>
- Park, J., Lühr, H., Lee, C., Kim, Y. H., Jee, G., & Kim, J.-H. (2014). A climatology of medium-scale gravity wave activity in the midlatitude/low-latitude daytime upper thermosphere as observed by CHAMP. *Journal of Geophysical Research: Space Physics*, *119*(3), 2187–2196. <https://doi.org/10.1002/2013JA019705>
- Perwitasari, S., Nakamura, T., Kogure, M., Tomikawa, Y., Ejiri, M. K., & Shiokawa, K. (2018). Comparison of gravity wave propagation directions observed by mesospheric airglow imaging at three different latitudes using the M-transform. *Annales Geophysicae*, *36*(6), 1597–1605. <https://doi.org/10.5194/angeo-36-1597-2018>
- Preusse, P., Dörnbrack, A., Eckermann, S. D., Riese, M., Schaeler, B., Bacmeister, J. T., et al. (2002). Space-based measurements of stratospheric mountain waves by CRISTA. I. Sensitivity, analysis method, and a case study. *Journal of Geophysical Research: Atmosphere*, *107*(D23), CRI 6–1–CRI 6–23. <https://doi.org/10.1029/2001JD000699>
- Sato, K., Watanabe, S., Kawatani, Y., Tomikawa, Y., Miyazaki, K., & Takahashi, M. (2009). On the origins of mesospheric gravity waves. *Geophysical Research Letters*, *36*, L19801. <https://doi.org/10.1029/2009GL039908>
- Song, I.-S., Lee, C., Chun, H.-Y., Kim, J.-H., Jee, G., Song, B.-G., & Bacmeister, J. T. (2020). Propagation of gravity waves and its effects on pseudomomentum flux in a sudden stratospheric warming event. *Atmospheric Chemistry and Physics*, *20*(12), 7617–7644. <https://doi.org/10.5194/acp-20-7617-2020>
- Song, I.-S., Lee, C., Kim, J.-H., Jee, G., Kim, Y.-H., Choi, H.-J., et al. (2017). Meteor radar observations of vertically propagating low-frequency inertia-gravity waves near the southern polar mesopause region. *Journal of Geophysical Research: Space Physics*, *122*(4), 4777–4800. <https://doi.org/10.1002/2016JA022978>
- Song, B.-G., Song, I.-S., Chun, H.-Y., Lee, C., Kam, H., Kim, Y. H., et al. (2021). Activities of small-scale gravity waves in the upper mesosphere observed from meteor radar at King Sejong Station, Antarctica (62.22°S, 58.78°W) and their potential sources. *Journal of Geophysical Research: Atmospheres*, *126*, e2021JD034528. <https://doi.org/10.1029/2021JD034528>
- Taylor, M. J., Ryan, E. H., Tuan, T. F., & Edwards, R. (1993). Evidence of preferential directions for gravity wave propagation due to wind filtering in the middle atmosphere. *Journal of Geophysical Research: Atmosphere*, *98*(A4), 6047–6057. <https://doi.org/10.1029/92JA02604>
- Vadas, S. L., Fritts, D. C., & Alexander, M. J. (2003). Mechanism for the generation of secondary waves in wave breaking regions. *Journal of the Atmospheric Sciences*, *60*(1), 194–214. [https://doi.org/10.1175/1520-0469\(2003\)060<0194:MFTGOS>2.0.CO;2](https://doi.org/10.1175/1520-0469(2003)060<0194:MFTGOS>2.0.CO;2)
- Zuev, V. V., & Savelieva, E. (2019). The cause of the strengthening of the Antarctic polar vortex during October–November periods. *Journal of Atmospheric and Solar-Terrestrial Physics*, *190*, 1–5. <https://doi.org/10.1016/j.jastp.2019.04.016>